Chaos and order in crossed fields

Jan von Milczewski and T. Uzer
School of Physics, Georgia Institute of Technology, Atlanta, Georgia 30332-0430
(Received 16 December 1996)

Atoms with a single highly excited electron (so-called Rydberg atoms), when placed in external fields, become atomic-scale laboratories in which the quantum mechanics of strongly nonlinear systems can be tested. Especially the extensive symmetry breaking introduced to the Coulomb potential by crossed electric and magnetic fields leads to rich nonlinear dynamics and is also a source of great complexity. In this paper, we analyze the nonlinear dynamics aspects of this atomic system, such as periodic orbits, bifurcations, order-chaos transitions, and islands of stability. In particular, we present an approximate Hamiltonian that turns out to be very effective in bringing out the classical structures that support the complexity of the motion. We conclude with a coherent state analysis that allows a direct comparison of quantum and classical results.
[S1063-651X(97)14705-5]

PACS number(s): 05.45.+b, 03.20.+i, 03.65.Sq

I. INTRODUCTION

The hydrogen atom in perpendicular (crossed) electric and magnetic fields is a classic problem of the early quantum theory [1]. However, in the intervening years, highly excited hydrogenic atoms (so-called Rydberg systems [2]) in external fields have emerged as atomic-scale laboratories where the quantum mechanics of classical chaotic systems can be tested [3]. In particular, Rydberg systems in crossed fields have become testing grounds for the quantum-mechanical signatures of three-dimensional chaotic motion [4,5].

The symmetry breaking of the Coulomb potential [6] induced by external fields affects the three quantum numbers n, l, and m_l of the Rydberg electron differently: as long as a single field direction is present, m_l remains a good quantum number, l breaks down extensively, whereas n breaks down only gradually with increasing magnetic field [3]. Therefore, an n manifold of electronic energy levels does not have enough degrees of freedom for chaos, which only develops when different n shells mix [7] (''intermanifold chaos''). In contrast, the extensive symmetry breaking introduced by two misaligned (in practice, crossed) fields causes ''intramanifold chaos.'' This chaos within an n manifold is a desirable scenario from an experimental point of view because, in principle, it can be tuned by varying the system parameters.

Of course, the full dynamics has three degrees of freedom and this feature causes much of the immense complexity of the dynamics. It is not easy to obtain an overview of the motion of a system with three degrees of freedom since phase space has six dimensions, and Poincaré surfaces of section are no longer useful. The high dimensionality of the crossed-fields problem opens the floodgates for a wealth of new physics, which is only possible beyond two degrees of freedom: for instance, Arnol'd diffusion can take place in this experimentally accessible system [8]. Less esoterically, it also becomes possible to form electronic wave packets localized in all spatial dimensions, and the observation of these wave packets, which was accomplished recently [9], opens an exciting window on the dynamics of the electron.

Using the ''old quantum theory'' and advanced methods of celestial mechanics, Pauli provided an elegant first-order solution to the crossed-fields problem as early as 1926, which emphasized how the solution progresses from a nondegenerate two-degree-of-freedom problem to a doubly degenerate one with two identical frequencies as the angle between the fields approaches 90° [1]. However, when the fields are strong, this solution is unable to describe the complex dynamics.

Recently, Gourlay *et al.* [10] have derived a Hamiltonian that describes the classical motion in the crossed-fields problem correct to second order in the fields. The purpose of this paper is to analyze the nonlinear dynamics aspects of this atomic problem using this approximate Hamiltonian, which turns out to be very effective in bringing out the classical structures that support the complexity of the motion. In particular, we will show that the most prominent periodic orbit, one that dominates the experimental results for a wide range of parameters [4,5], emerges naturally as the most stable orbit in our analysis.

This paper is organized as follows. In Sec. II, we introduce the approximate Hamiltonian, and we describe its symmetries and scaling properties. We apply perturbation theory to reduce the dimensionality of this problem. In Sec. III, we present the structure of phase space generated from the approximate Hamiltonian. Special attention is given to a stability analysis (Sec. IV), revealing interesting chaos-order alternations that indicate the existence of approximate constants of motion. These results are compared with the exact motion. Section V compares quantum mechanical properties of the approximate Hamiltonian with our classical findings. The work is summarized in Sec. VI.

II. PERTURBATION THEORY

Neglecting relativistic effects, the motion of an electron in perpendicular electric and magnetic fields is described by the perturbed Coulomb Hamiltonian [11]

$$H=\frac{1}{2}\mathbf{p}^2+\frac{B}{2}L_z+\frac{B^2}{8}(x^2+y^2)-\frac{1}{r}+Fx. \qquad (1)$$

We use atomic units throughout, i.e., the magnetic field B is given in units of $B_0=(e/\hbar)^3 m_e^2 c=2.35\times 10^5$ T and points in

the z direction whereas the electric field F is in units of $F_0=e^5m_e^2/\hbar^4=5.14\times10^{11}$ V/m and points in the x direction. In the remaining part of this paper we will refer to the dynamics induced by Hamiltonian (1) as *exact* as opposed to the *approximate* treatment outlined below.

In this section we will only sketch the derivation of the approximate Hamiltonian and refer the reader interested in the details to Ref. [10]. The regularization of Hamiltonian (1) in the four Kustaanheimo-Stiefel coordinates $\mathbf{u}$ and their conjugate momenta $\mathbf{P}_u$ leads to the pseudo-Hamiltonian

$$\mathcal{H}=\frac{4}{\omega}=\frac{1}{2}(\mathbf{P}_u^2+\mathbf{u}^2)+\frac{2}{\omega^2}BL_z\mathbf{u}^2+2\frac{B^2}{\omega^4}\mathbf{u}^2(u_1^2+u_4^2)(u_2^2+u_3^2)+\frac{8F}{\omega^3}\mathbf{u}^2(u_1u_3+u_2u_4), \tag{2}$$

where

$$\omega=\sqrt{-8E}$$

and L_z is the z component of the electronic angular momentum $\mathbf{L}=\mathbf{r}\times\mathbf{p}$.

A useful view on the dynamics of Hamiltonian (2) is given by the following set of canonical variables:

$$L_z=\frac{1}{2}(I_b+I_d),\quad \phi_{L_z}=\phi_b+\phi_d,$$

$$A_z=\frac{1}{2}(I_b-I_d),\quad \phi_{A_z}=\phi_b-\phi_d,$$

$$n=\frac{1}{2}(I_a+I_c),\quad \phi_n=\phi_a+\phi_c,$$

$$\Delta_{L_z}=\frac{1}{2}(I_a-I_c),\quad \phi_{\Delta_{L_z}}=\phi_a-\phi_c, \tag{3}$$

where the action variables $I_a,\ldots,I_d$ and their conjugate angles $\phi_a,\ldots,\phi_d$ have been introduced in [10]. The conserved quantity Δ_{L_z} and its conjugate angle $\phi_{\Delta_{L_z}}$ are due to the introduction of a fourth degree of freedom by the Kustaanheimo-Stiefel transformation, and the physical motion may be recovered by requiring $\Delta_{L_z}=0$. The quantity n is the classical analog to the principal quantum number, given also by the harmonic oscillator part of Hamiltonian (2):

$$2n=\tfrac{1}{2}(\mathbf{P}^2+\mathbf{u}^2). \tag{4}$$

A. Reduced dimensionality Hamiltonians

When the normal form resulting from the classical perturbative treatment is expressed in terms of the two angular momenta $\mathbf{J}$ and $\mathbf{K}$, the Lie-algebraic generators of the group SU(2)⊗SU(2), isomorphic to the symmetry group SO(4) of the Coulomb problem [12],

$$\mathbf{J}=(\mathbf{L}+\mathbf{A})/2,\ \mathbf{K}=(\mathbf{L}-\mathbf{A})/2, \tag{5}$$

it contains a pair of degenerate, strongly coupled asymmetric tops in these two generators:

$$E^{(2)}=-\frac{1}{2n^2}+\frac{B}{2}(J_z+K_z)-\frac{3Fn}{2}(J_x-K_x)+\frac{B^2n^2}{16}[3n^2-4(J_z^2+K_z^2-J_zK_z)-8(J_xK_x+J_yK_y)]+\frac{F^2n^4}{16}[-17n^2+12(J_x^2+K_x^2+J_xK_x)]-\frac{FBn^3}{2}(J_zK_x-J_xK_z). \tag{6}$$

In the following, we will refer to this Hamiltonian as *normalized*. Here, $\mathbf{A}$ is the Runge-Lenz-Laplace vector, which indicates the semimajor axis of the elliptic orbit in the Kepler-Coulomb problem. $\mathbf{A}$ is given by [13]

$$\mathbf{A}=\frac{1}{\sqrt{-2H_0}}\left(\mathbf{p}\times\mathbf{L}-\frac{\mathbf{r}}{r}\right), \tag{7}$$

where

$$H_0=\frac{\mathbf{p}^2}{2}-\frac{1}{r} \tag{8}$$

is the energy of the field-free motion.

The vectors $\mathbf{J}$ and $\mathbf{K}$ have the norm $n/2$, which is a conserved quantity in our treatment, making Hamiltonian (6) effectively two dimensional. The third degree of freedom is represented by n and its canonically conjugate angle ϕ_n.

The vectors $\mathbf{J}$ and $\mathbf{K}$ obey the angular momentum Poisson bracket relations, and the equations of motion may be found from

$$\frac{d}{dt}\mathbf{J}=[\mathbf{J},H]=\nabla_{\mathbf{J}}H\times\mathbf{J}, \tag{9}$$

and correspondingly for $(d/dt)\mathbf{K}$, with $H=E^{(2)}(\mathbf{J},\mathbf{K})$. By $[,]$ we denote the Poisson bracket, and $\nabla_{\mathbf{J}}$ denotes the differentiation with respect to (J_x,J_y,J_z).

We will rely on the normalized Hamiltonian (6) to analyze the motion in this system.

However, it is possible to perform a further approximation to smooth out the chaos [14]. A pair of rotations, one for $\mathbf{J}$,

$$\begin{pmatrix}\tilde{J}_x\\ \tilde{J}_y\\ \tilde{J}_z\end{pmatrix}=\frac{1}{\sqrt{1+a^2}}\begin{pmatrix}1&0&a\\0&1&0\\-a&0&1\end{pmatrix}\begin{pmatrix}J_x\\J_y\\J_z\end{pmatrix}, \tag{10}$$

where

$$a=\frac{3nF}{B}, \tag{11}$$

and a corresponding one of $\mathbf{K}\rightarrow\tilde{\mathbf{K}}$ with the transpose of the matrix in Eq. (10) is needed to simplify the linear terms in Hamiltonian (6) to

$$\widetilde{E}^{(1)} = -\frac{1}{2n^2} + \omega_L \widetilde{L}_z, \tag{12}$$

where $\widetilde{\mathbf{L}} = \widetilde{\mathbf{J}} + \widetilde{\mathbf{K}}$, $\widetilde{\mathbf{A}} = \widetilde{\mathbf{J}} - \widetilde{\mathbf{K}}$.

Averaging over the linear motion, which is harmonic with the frequency $\omega_L = \frac{1}{2}\sqrt{B^2 + (3nF)^2}$, results in an integrable approximation [14]:

$$\widetilde{E}_{ad}(\mathbf{J},\mathbf{K}) = \widetilde{E}^{(1)} + C + \frac{n^2}{128\omega_L^2}[\delta_1 n^2 + \delta_2(\widetilde{J}_z + \widetilde{K}_z)^2 + \delta_3(\widetilde{J}_z - \widetilde{K}_z)^2 - \delta_4(\widetilde{J}_x\widetilde{K}_x + \widetilde{J}_y\widetilde{K}_y)], \tag{13}$$

where

$$C = \frac{3B^2n^4}{16} - \frac{17F^2n^4}{16}, \tag{14}$$

$$\delta_1 = -12B^2F^2n^2,$$

$$\delta_2 = -2B^4 + 24B^2F^2n^2 + 54F^4n^4,$$

$$\delta_3 = -6B^4 + 162F^4n^4,$$

$$\delta_4 = 16B^4 + 144B^2F^2n^2. \tag{15}$$

Hamiltonian (13) is equivalent to the second-order quantal perturbative treatment [15]. An analysis of Hamiltonian (13) shows that three adiabatic invariants determine the physics, or more specifically the invariant tori, namely, $n, \widetilde{L}_z$, and Ω, which are constants of motion generated by Hamiltonian (13) [14],

$$\widetilde{L}_z = \widetilde{J}_z + \widetilde{K}_z, \tag{16}$$

$$\Omega = \gamma(\widetilde{J}_z - \widetilde{K}_z)^2 - 4(\widetilde{J}_x\widetilde{K}_x + \widetilde{J}_y\widetilde{K}_y), \tag{17}$$

where

$$\gamma = 4\frac{\delta_3}{\delta_4} = -\frac{3}{2} + \frac{a^2(3+a^2)}{2(1+a^2)}, \quad -\frac{3}{2} \leqslant \gamma < \infty. \tag{18}$$

B. Symmetries and scaling

Hamiltonian (1) is symmetric with respect to reflections at the xy plane (parity) and with respect to the operation $y \to -y$, $p_x \to -p_x$, $p_z \to -p_z$, which induces a generalized time reversal symmetry [16]. For the approximate Hamiltonians, these operations correspond to $(J_x, J_y, J_z) \leftrightarrow (-K_x, -K_y, K_z)$ for parity, and $(J_y, K_y) \to (-J_y, -K_y)$ for time reversal symmetry.

Due to the parity symmetry, trajectories that are started with $z = p_z = 0$ will always remain in the xy plane. This planar motion appears to be most important for the semiclassical analysis of the quantum spectra [4,5].

For $F = 0$, L_z is a constant of the motion, whereas for $B = 0$, L_x is a constant of the motion, making the normalized Hamiltonian integrable in these cases. It follows that for $B \ll F$ and $F \ll B$ the normalized motion becomes regular.

A very important and helpful property of Rydberg systems in external fields is the scaling of their classical dynamics with respect to the external parameters [3]. In our approximate treatment, the quantity n is conserved and may be regarded as an additional external parameter (this is the price that one has to pay in reducing this system from 3 to 2 degrees of freedom). It is more convenient to use the scaling of the system with respect to n instead of the usual scaling with the magnetic field [3].

Calculations done with a fixed n may be transferred to the dynamics for $n \neq 1$ by scaling

$$B/n^3, \quad F/n^4, \tag{19}$$

$$tn^3, \quad E/n^2, \tag{20}$$

$$\mathbf{J}n, \quad \mathbf{K}n, \tag{21}$$

$$\mathbf{r}n^2, \quad \mathbf{p}/n. \tag{22}$$

Quantum mechanically, constant n means that we remain within one n manifold. In the following we will use $n = 1$ for convenience unless otherwise noted.

III. THE STRUCTURE OF PHASE SPACE

The perturbation Hamiltonian (6) shows that the motion of an electron in crossed fields is composed of two parts, which are decoupled by perturbation theory: For short times the electron moves on a Kepler ellipse. The fast motion along this ellipse is given by the angle ϕ_n conjugate to n. The external fields cause the elements of the ellipse, represented by **J** and **K**, to evolve slowly in time. This evolution is very well described by the normalized Hamiltonian (6), and it is the main subject of this paper.

The interplay of fast and slow motion and the simplification brought about by the normalized Hamiltonian are depicted in Fig. 1: the complicated motion in Cartesian coordinates [Fig. 1(a)] includes the fast Kepler motion. Plotting the same orbit in **JK** space (so-called rotor coordinates) eliminates the fast motion. The normalized motion may then be understood as averaging over the fast Kepler motion.

One can expect the averaging to be valid as long as the two frequencies are sufficiently separated, i.e.,

$$\omega_{\text{Kepler}} = \frac{\partial E}{\partial n} \approx \frac{1}{n^3} \gg \omega_L = \frac{1}{2}\sqrt{B^2 + (3nF)^2}. \tag{23}$$

Here, ω_L is the frequency of the first-order motion of the rotors **J** and **K**.

The general structure of phase space imposed by the normalized Hamiltonian is expected to remain robust for high fields. However, important limitations are imposed by the inability of the normalized Hamiltonian to describe n mixing and ionization.

In what follows, the structure of phase space generated by the normalized Hamiltonian (6) is presented under several headings and compared to the exact motion as appropriate.

A. Poincaré surfaces of section

For the normalized Hamiltonian with effectively two degrees of freedom, Poincaré surface of section (PSOS) plots constitute a valuable tool in displaying the structure of phase

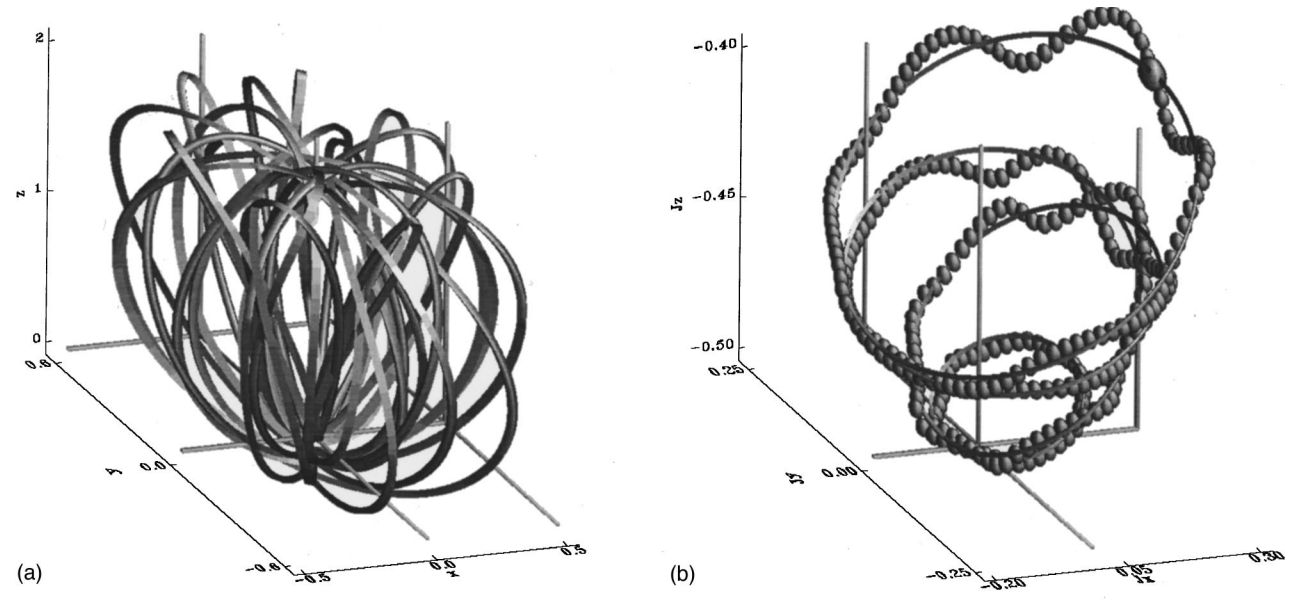

FIG. 1. A striking example of the simplifications introduced by our treatment: (a) a periodic orbit with 23 loops in Cartesian coordinates and (b) three loops in rotor coordinates. In (b), the exact **J** motion (the trajectory is displayed using balls) is compared to the normalized motion (solid).

space. From symmetry considerations we chose $K_y=0$ and $(d/dt)K_y>0$ as the surface of section.

Since the vectors **J** and **K** are restricted to a sphere, it would be ideal to plot PSOS's on a sphere. However, in order to plot it on a plane, we project this sphere by choosing the canonically conjugate variables

$$q_J=\frac{2J_x}{\sqrt{n-2J_z}}, \quad p_J=-\frac{2J_y}{\sqrt{n-2J_z}},$$

$$q_K=-\frac{2K_x}{\sqrt{n-2K_z}}, \quad p_K=\frac{2K_y}{\sqrt{n-2K_z}}. \tag{24}$$

These equations may be reversed:

$$J_x=\frac{q_J}{2}\sqrt{2n-q_J^2-p_J^2}, \quad K_x=-\frac{q_K}{2}\sqrt{2n-q_K^2-p_K^2},$$

$$J_y=-\frac{p_J}{2}\sqrt{2n-q_J^2-p_J^2}, \quad K_y=\frac{p_K}{2}\sqrt{2n-q_K^2-p_K^2},$$

$$J_z=\frac{1}{2}(q_J^2+p_J^2-n), \quad K_z=\frac{1}{2}(q_K^2+p_K^2-n). \tag{25}$$

Figure 2 shows some typical PSOS plots. Exploiting the time reversal symmetry, we show the upper half of each plot only. The ''hole'' in the PSOS plot in Fig. 2(d) is energetically not accessible.

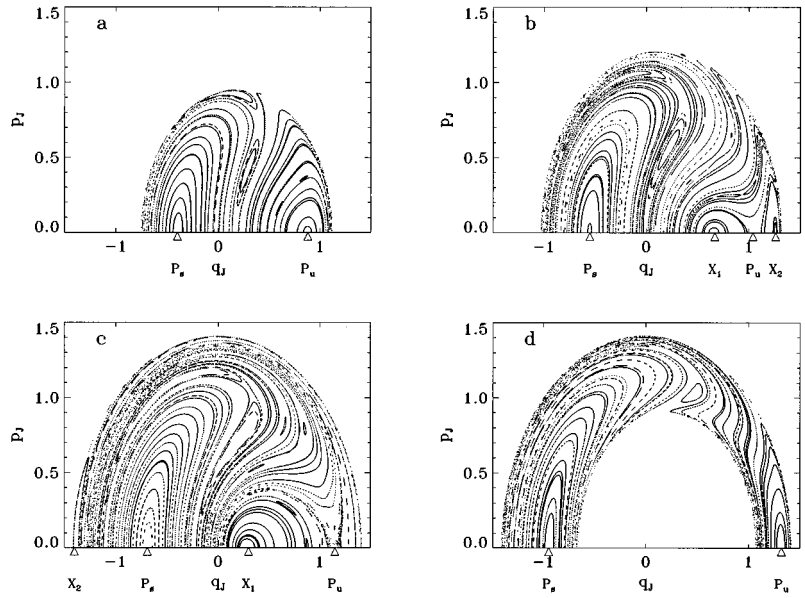

FIG. 2. Typical Poincaré surface of section plots for the normalized motion. The fields are fixed at $B=0.40$, $F=0.05$. The energy is $E=-0.60$, -0.55, -0.50, -0.40 [(a)–(d)]. The positions of the four basic periodic orbits are indicated. Because of symmetry, only one-half of each surface of section needs to be displayed.

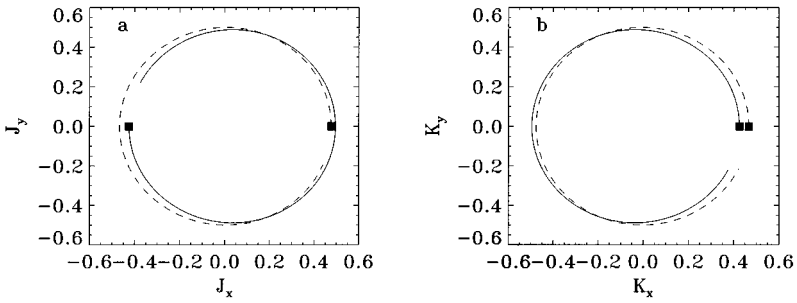

FIG. 3. The two orbits P_s (solid) and P_u (dashed) in the normalized motion for the parameters of Fig. 2(c). We show their projection onto (a) the J_xJ_y plane and (b) the K_xK_y plane. The starting point is marked by a square, and, in order to show their sense of rotation, the orbits are not completely closed.

The PSOS plots in Fig. 2 show that the motion may become chaotic for intermediate energies (around $E=-1/2n^2$). But for the fields chosen here the motion is mostly regular and the structuring of phase space by invariant tori is clearly visible.

One can also see that the principal tori intersect the symmetry line $p_J=p_K=0$ (i.e., $J_y=K_y=0$). Thus, we can obtain the important features of phase space by launching trajectories along this line only, varying, as we do here, q_J, while q_K is adapted to match the desired energy. These initial conditions will be used in the next section. What is more, those periodic orbits that result from the breakup of the field-free tori, being symmetric with respect to the time reversal symmetry, are located on $J_y=K_y=0$ with $(d/dt)K_y>0$ or $(d/dt)K_y<0$.

At least for small fields, it is useful to plot PSOS's for the exact (i.e., three dimensional) motion using the variables above. For higher fields, the coupling to the third degree of freedom becomes more important and the torus structure in this projection on two degrees freedom becomes more and more fuzzy.

B. Four basic periodic orbits

The PSOS plots in Fig. 2 show that the structure of phase space generated from the normalized Hamiltonian (6) is dominated by four fixed points on the line $p_J=p_K=0$, corresponding to four one-loop (in **JK** space) periodic orbits, which we call P_s, P_u, X_1, and X_2.

The orbits P_s and P_u (displayed in Fig. 3) exist for all field strengths and energies examined. For P_s, we have along the orbit

$$(J_x,J_y,J_z)=(-K_x,-K_y,K_z), \tag{26}$$

which is equivalent to $L_x=0, L_y=0, A_z=0$. This corresponds to the motion in the xy plane $z=p_z=0$, and P_s is totally symmetric with respect to parity. These conditions allow one to solve for the trajectory's orbit analytically. For P_u we have

$$(J_x,J_y,J_z)|_t=(-K_x,-K_y,K_z)|_{t+T/2}, \tag{27}$$

where T is the orbit's period.

For intermediate energies and small electric fields [as in Fig. 2(b)], P_u becomes unstable and bifurcates into the two stable orbits X_1 and X_2, which are related by the parity symmetry. Significantly, chaos spreads from this region of instability.

P_s is very stable here; it may become unstable only for electric fields that are strong compared with the magnetic field (see also Sec. IV E), in the process generating two stable periodic orbits, which we also call X_1 and X_2.

An analysis in terms of the adiabatic invariants $\tilde{L}_z$ and Ω [Eqs. (16) and (17)] shows that P_u becomes unstable for [14]

$$\gamma<-1\Leftrightarrow a<0.644\Leftrightarrow Fn<0.215B, \tag{28}$$

i.e., for high magnetic fields (relative to the electric field), while P_s becomes unstable for

$$\gamma>1\Leftrightarrow a<1.857\Leftrightarrow Fn<0.619B, \tag{29}$$

i.e., for high electric fields.

The position and stability of more complicated periodic orbits in the normalized motion are shown in the figures in Sec. IV.

C. Periodic orbits of the exact motion

The normalized Hamiltonian facilitates the search for periodic orbits of the exact motion where the periodicity of $\mathbf{J}(t)$ and $\mathbf{K}(t)$ is a necessary condition for periodicity of an orbit of the exact motion. In addition, the Kepler motion along ellipses, given by ϕ_n, has to be taken into account, which can often be achieved by adjusting the initial angle of ϕ_n. The smaller the fields, the more loops are introduced by the inclusion of ϕ_n because the **JK** motion becomes slower with respect to the fast motion.

Thus, finding periodic orbits in the exact motion from a periodic orbit in the normalized motion is a two-step process. After finding the periodic **JK** motion, it is often possible to make the orbit close on itself (i.e., ϕ_n has to go through multiples of 2π) by merely varying the starting angle $\phi_n(0)$. In view of the complicated structure of the motion in a six-dimensional phase space, this is a remarkable simplification.

When the motion contained in the robust fixed point (P_s) is translated to Cartesian coordinates in this way, it turns out to be the one planar periodic orbit (denoted by C_1 by Raithel *et al.* [4]) that dominates most of their photoabsorption spectra (see Fig. 4). In our description, the prominence of this orbit is clearly connected to the stability of the motion, and its special status is evident at once, proving that both the action-angle variables we use, as well as the approximate Hamiltonian, are the most appropriate for this problem.

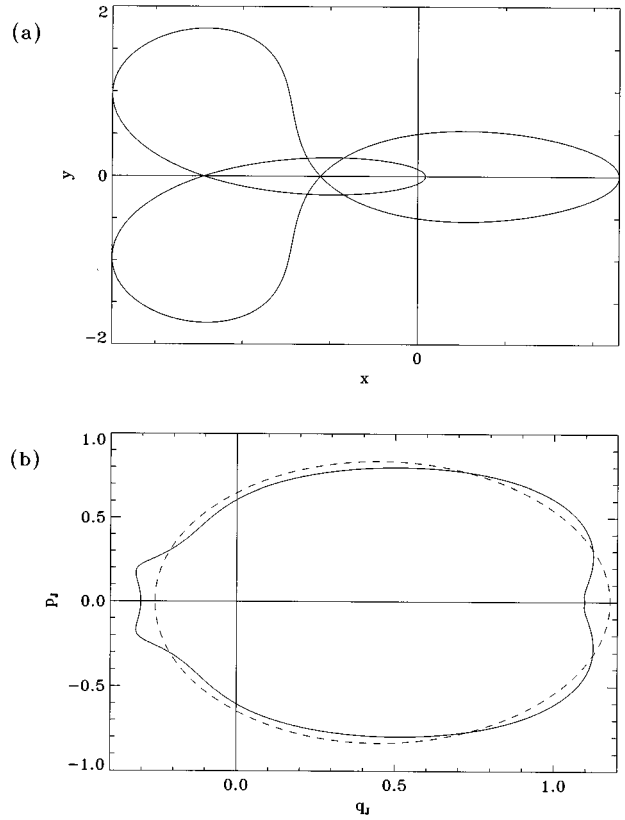

FIG. 4. Periodic orbits P_s in the exact motion. (a) The motion is bound to the xy plane. (b) shows a comparison of the exact (solid) **J** motion (in terms of q_J and p_J) with the normalized motion (dashed).

D. Phase difference

Figure 3 shows that P_s and P_u are rotating in the same direction. They differ mainly by their phase difference between the **J** and the **K** rotor (projected onto the xy plane), which is π for P_s and 0 for P_u. This can also be seen from Eqs. (26) and (27).

To see what this means for the structure of phase space, we have computed an average phase difference for arbitrary trajectories. For a point on a trajectory, the phase difference may be defined as the angle $\delta_{JK}=\delta_J-\delta_K$, where $\tan\delta_J=dJ_x/dJ_y$ is the direction of the trajectory in the J_xJ_y plane, and δ_K is defined correspondingly. Computing the average value of the angle δ_{JK} requires computing the average values of its sine and cosine.

In Fig. 5 we have plotted the average value of δ_{JK} along trajectories started on the line $p_J=p_K=0$. One can see that phase space is dynamically separated into two regions around P_s and P_u with an average phase difference of 0 and π, respectively. This behavior is not restricted to the special initial conditions $p_J=p_K=0$. In parameter regimes with widespread chaos, the trajectory may jump between the two domains.

It should be noted that the average phase difference becomes interesting only by the coupling of the rotors through the second-order terms in Hamiltonian (6). In the first-order motion, the phase difference is merely a constant, and may acquire any value.

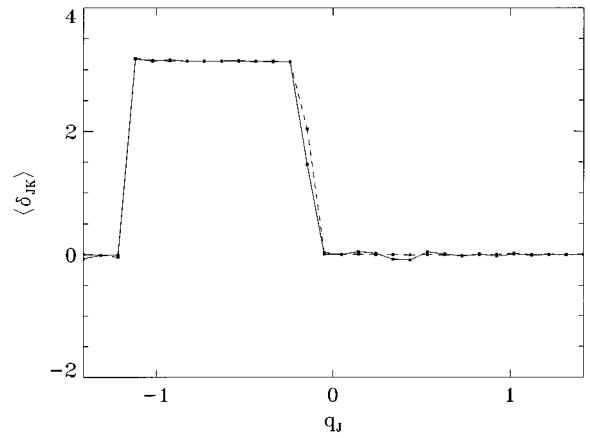

FIG. 5. Average phase difference $\langle\delta_{JK}\rangle$ along the line $p_J=p_K=0$ as a function of q_J for the exact (solid) and the normalized (dashed) motion; the external parameters are the same as in Fig. 2(c).

IV. STABILITY ANALYSIS

A. Intramanifold chaos

Another interesting view onto phase space is given by a stability analysis, specifically in terms of Lyapunov stability. Figure 2 reveals that for intermediate energies, the orbit P_u becomes unstable. Chaos spreads from this region of instability and becomes strongest for energies around $-\frac{1}{2}$, whereas the motion in an n manifold is regular for low and high energies. Because n is fixed (or approximately conserved in the exact motion), the chaotic motion described here may be termed intramanifold chaos [17]. This is to be compared with the case of a pure magnetic field (the quadratic Zeeman effect [3,18]), where, due to the conservation of L_z, an n manifold does not have enough degrees of freedom for chaos. The latter problem shows significant chaos only when different n manifolds mix.

The transition from order to chaos and back can be shown in a more compact way: we restrict ourselves to trajectories starting on the line $p_J=p_K=0$ (see Sec. III A) and plot the maximum Lyapunov exponent as a function of E and q_J (Fig. 6). The maximum Lyapunov exponent has been computed by following the separation of nearby trajectories over a finite time interval. Thus, for regular orbits the Lyapunov exponent is positive but small (this value depends mainly on B and F, and on the time interval chosen), but it is clearly separated from the Lyapunov exponents of trajectories in chaotic regions.

In addition, in Fig. 6 we show the positions of periodic orbits with up to four loops in the rotor coordinates. The periodic orbits P_s and P_u can be seen to extend from the minimum to the maximum energy. For intermediate energies, P_u bifurcates and becomes unstable (Fig. 6), generating the X_1,X_2 orbits. More complicated orbits bifurcate from this pair of orbits. They get squeezed together around P_u, thus creating chaos via overlapping resonances.

A Lyapunov analysis of the exact motion [Fig. 6(b)] shows the same regions of instability. The chaos we see here is related to the evolution of **J** and **K**. For the fields considered here it shows little dependence on the third degree of freedom (ϕ_n), which is neglected here and in what follows.

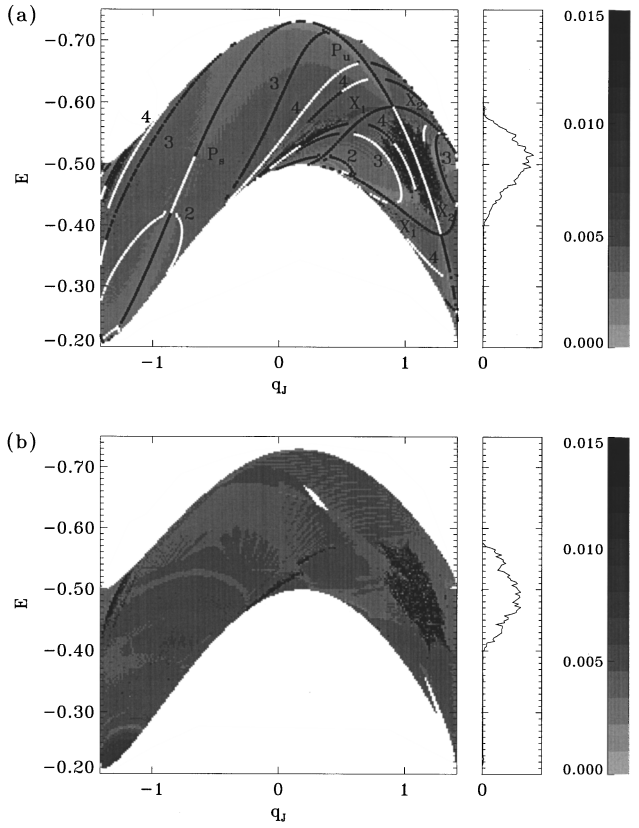

FIG. 6. Stability analysis as a function of the energy at $B=0.5$, $F=0.05$ along the symmetry line $p_J=p_K=0$: comparison of the normalized (a) **J** motion with the (b) exact motion. The shading is chosen according to the value of the maximum Lyapunov exponent, dark regions denoting chaotic motion. The smaller panels on the right-hand side show the average Lyapunov exponent along horizontal lines; numerical Lyapunov exponents below a small threshold are neglected. In addition, in (a), we indicate the positions of periodic orbits with up to four loops in the normalized motion, distinguishing between stable (black) and unstable (white) motion.

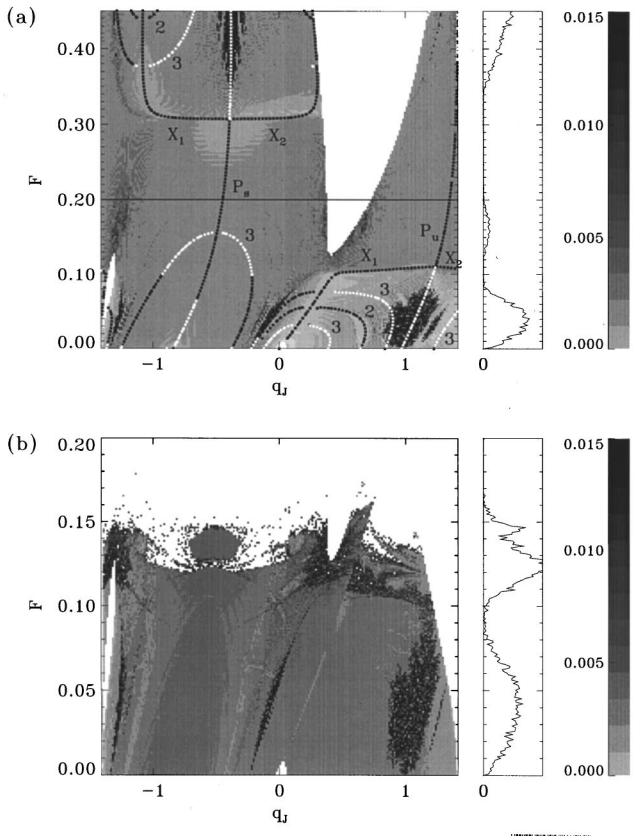

FIG. 7. Stability analysis of (a) the normalized and (b) the exact motion as in Fig. 6, now as a function of the electric field F at $E=-\frac{1}{2}$, $B=0.5$. Here, only periodic orbits with up to three loops are marked. Note the different scales in (a) and (b): in the exact motion strong ionization sets in for electric fields above $F\approx 0.15$ and the maximum value of F in this panel is at $F=0.2$, which is marked by a line in (a).

B. Variation with the fields

Investigating different values of F, one finds that the bifurcation of P_u into X_1 and X_2 fails to take place for higher F values [see also Eq. (28)]. As a consequence, there is no chaos visible for these F values.

This behavior can be investigated through a plot similar to Fig. 6, fixing the energy at $E=-\frac{1}{2}$ and varying F [Fig. 7(a)]. For low but finite F, P_u is unstable and a considerable fraction of phase space is chaotic. We find that even a rather small electric field enhances chaos considerably with respect to the quadratic Zeeman effect (in the absence of F). At $F\approx 0.11$, the orbits X_1 and X_2 vanish, and P_u becomes stable, making the overall motion much more regular.

At yet higher F (or lower B with respect to F), P_s bifurcates in an analogous way, giving rise to strong chaos surrounding it. Thus the stability of the overall motion is very much dictated by the stability of the two orbits P_s and P_u. Note, however, that the chaotic region generated by the instability of P_s in Fig. 7(a) is beyond the ionization threshold now. Up to $F\approx 0.9$, the agreement with the exact motion is very good.

The correlation of short unstable periodic orbits with the location of chaotic regions becomes evident again if we investigate how the stability depends on the magnetic field (Fig. 8). We chose to display this for the *intermediate* energy $E=-\frac{1}{2}$, which appears to show most widespread chaos. One recognizes again that even for larger fields, the approximate treatment reproduces well the location of chaotic regions. Visible changes in the structure of chaotic regions appear only around $B=0.9$. On the average, the extent of chaotic regions grows with B.

C. Lines of stability

Further windows on the dynamics are opened by examining the percentage of chaotic trajectories as a function of electric and magnetic fields. To this end, we computed a large number of trajectories throughout the surface of section for each value of B and F. As a measure of chaos, we use the average value of the maximum Lyapunov exponent (the Kolmogorov-Sinai entropy [19]). One can show that for this problem to first order in the fields, equal areas on the SOS represent equal volumes in phase space.

The most striking feature seen in Fig. 9 is a ''ridge of stability'' at $F/B\approx 4/7$, which penetrates a large chaotic area. On this line, the PSOS becomes very regular [e.g., Fig. 10(g)]. Note that chaos is strongest just below this line, while

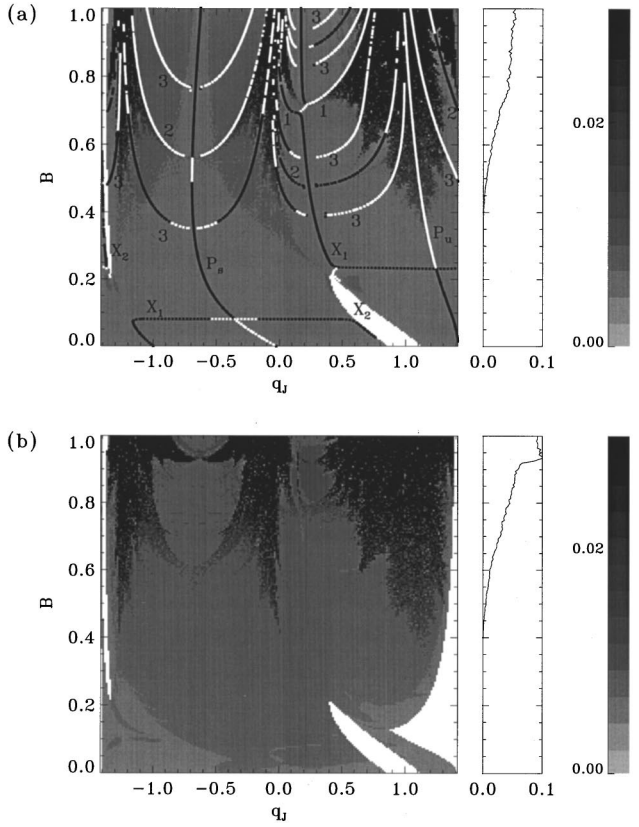

FIG. 8. Stability analysis of (a) the normalized and (b) the exact motion as in Fig. 6, now as a function of the magnetic field B at $E=-\frac{1}{2}, F=0.05$. Here, only periodic orbits with up to three loops are marked.

for $F\to 0$ and $B\to 0$ the normalized motion becomes regular, as expected.

At $F/B\approx 1/5$, another line of stability can be detected, but it is much weaker than the first one. These remarkable alternations between order and chaos are pictured by a series of PSOS plots in Fig. 10 where only the electric field is changed. The two lines of stability occur close to the field values where the second order quantum perturbation expression becomes separable [20].

D. Numerical constants of the motion

The lines of stability may be made visible in yet another way by starting from the fact that regular motion is associated with the existence of approximate constants of the motion. One can try numerically to find a constant of the motion by assuming it to be in the form of a polynomial p in some dynamical variables with free coefficients that are to be computed by a fitting procedure. Trajectories are started on a grid throughout phase space and integrated for a number of time steps. The coefficients are determined so as to minimize the mean squared deviation of p along each trajectory from the average of p for that trajectory. To exclude the trivial zero solution, one point on each trajectory is chosen to be close to a quantity characteristic for that trajectory like the average of a dynamical variable. The normalized mean deviation σ of p from constancy averaged over all trajectories indicates the quality of the numerical constant of the motion.

In Fig. 11 we plot σ for a polynomial p in J_x, J_z, K_x, and K_z as a function of the electric field F. The weak line of stability is visible only for a polynomial of third order while the strong line of stability shows itself in both cases. Both the second- and the third-order polynomial perform mostly better than the analytic adiabatic invariant Ω [Eq. (17)]. Plotting σ as a function of B and F for a third-order polynomial reveals the existence of the lines of stability for very low fields as well.

The procedure described here does not appear to be applicable to the exact (three degrees of freedom) motion.

E. Stability of the planar motion

As mentioned above, the orbit P_s represents the motion in the xy plane, and its stability becomes an indicator for the stability of the exact motion with respect to the xy plane. To demonstrate this, in Fig. 12, we have plotted the Lyapunov stability of P_s in the normalized motion and the maximum distance to the xy plane for an arbitrary orbit of the exact motion initially close to the xy plane: when the motion with respect to xy plane becomes unstable, such an orbit will repeatedly move away exponentially fast from the xy plane and return to it symmetrically.

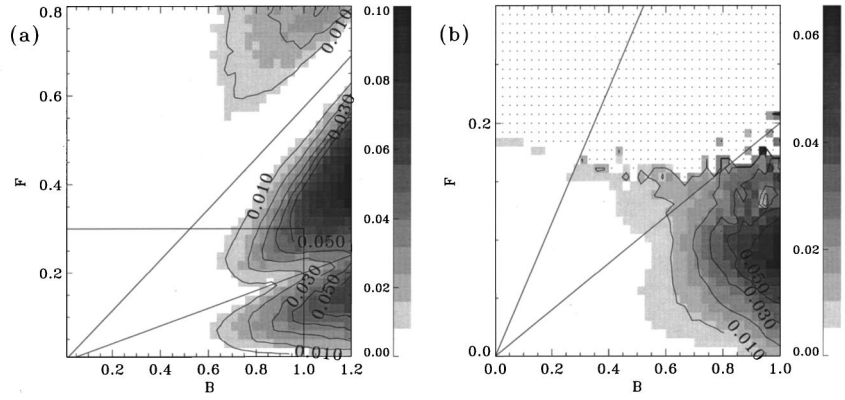

FIG. 9. Kolmogorov-Sinai entropy for (a) the normalized and (b) the exact motion as a function of B and F, showing the two ridges of stability (marked by two lines). In the exact motion the strong line of stability cannot be detected due to the onset of ionization. In this figure, dark regions denote regions with predominantly chaotic motion. In the dotted areas in (b), only ionizing trajectories were found. In (b), the field values are restricted to the box drawn in (a).

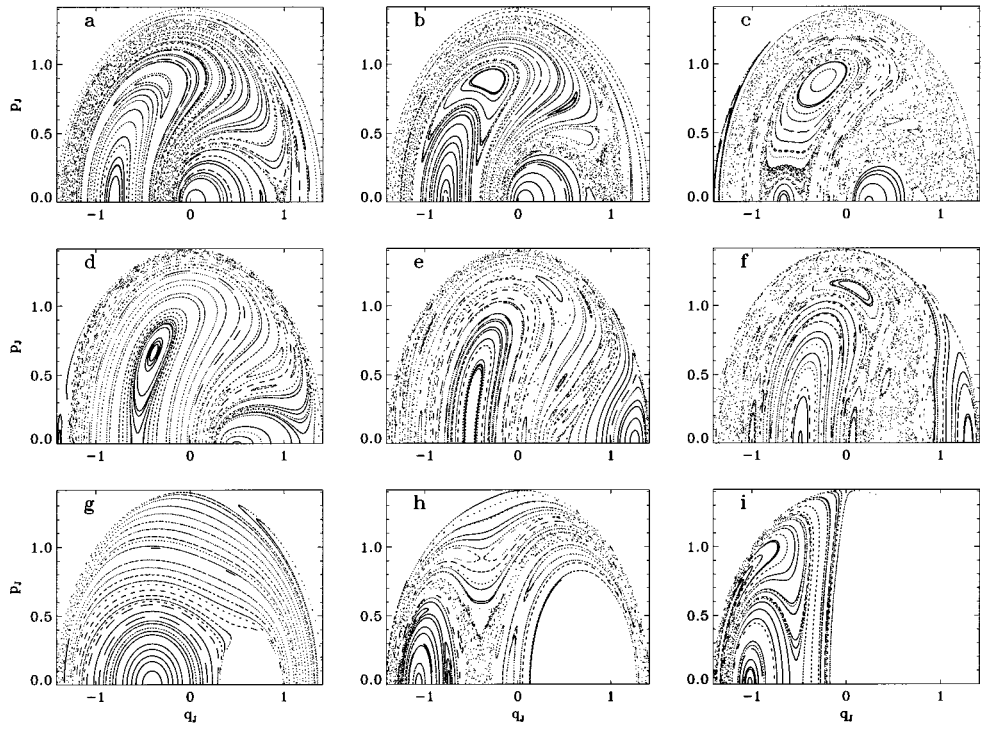

FIG. 10. Surface of section plots for the normalized motion showing repeated transitions from order to chaos and back at $E=-\frac{1}{2}$, $B=0.6$, and $F=0.001$ (a), 0.01 (b), 0.06 (c), 0.12 (d), 0.15 (e), 0.18 (f), 0.34 (g), 0.60 (h), and 1.00 (i).

Both panels show that the motion with respect to the xy plane becomes unstable approximately for $F>0.62B$ when P_s becomes unstable due to the bifurcation into X_1 and X_2. There is another region of instability around $B=0.55$, which occurs after a two-loop periodic orbit has bifurcated from P_s. A third region of instability in the exact motion, at yet higher B, is not reproduced by the normalized Hamiltonian.

V. QUANTUM MECHANICS

A. Diagonalization of the approximate Hamiltonian

In this section, we will discuss some of the quantum mechanical properties of Hamiltonian (6) that can be quantized by replacing **J** and **K** by their corresponding angular momentum operators. Hamiltonian (6) is diagonalized in each n manifold ($n=1,2,\ldots$) in a basis consisting of products of eigenstates of the angular momenta **J** and **K**:

$$|m_J m_K n\rangle = |j m_J\rangle |k m_K\rangle, \tag{30}$$

where $j=k=(n-1)/2$ and $m_J, m_K = -(n-1)/2, -(n-1)/2+1, \ldots, (n-1)/2$. The parity symmetry may be used by selecting the linear combinations

$$|m_J m_K, \pm\rangle = (|m_J m_K\rangle \pm |m_K m_J\rangle)/\sqrt{2}, \tag{31}$$

$m_J \geqslant m_K$ ($m_J > m_K$ for "$-$"), which have the parity $\pm(-1)^{(m_J+m_K)}$.

As the basis is finite for fixed n (of dimension n^2) and all the integrals may be evaluated algebraically, the exact energy levels may easily be computed (with very small numerical errors). For given n, the Hamilton matrix is banded with bandwidth $2n+1$ provided the basis is ordered appropriately; thus it is possible to go up to very high values of n.

To compare these approximate eigenstates with the eigenstates of the exact motion, we have computed some low-lying energy levels of Hamiltonian (1) by diagonalizing the Hamilton matrix in a basis of Sturmian functions [21]. We found the energy levels to be correct to at least second order in the fields, i.e., the error scales like ϵ^3 (for some levels like ϵ^4) when $B=\epsilon b$ and $F=\epsilon f$, where b and f are fixed.

The latter is true only after adding two constant terms (known from the single field theories) to the normalized Hamiltonian (6), namely, $B^2n^2/16$ [22] and $19F^2n^4/16$ [23]. In the semiclassical limit of high n, these terms are small with respect to the remaining second-order terms.

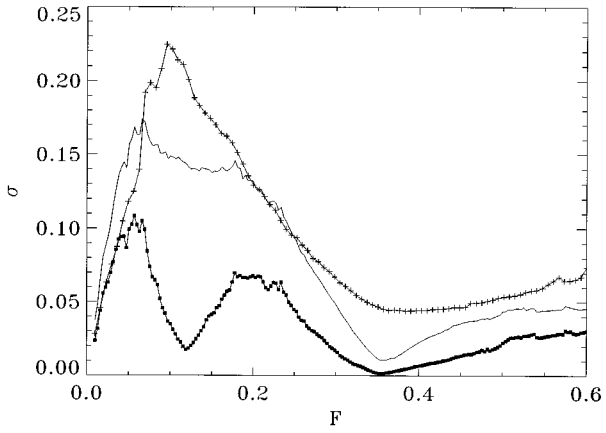

FIG. 11. Quality of the fit of a numerical approximate constant of the motion as a function of F at $E=-\frac{1}{2}$ and $B=0.6$. The curve marked by squares has been generated by a fit of a third-order polynomial, the solid curve is for a second-order polynomial. We also show the quality of the adiabatic invariant Ω [Eq. (17)] (crosses).

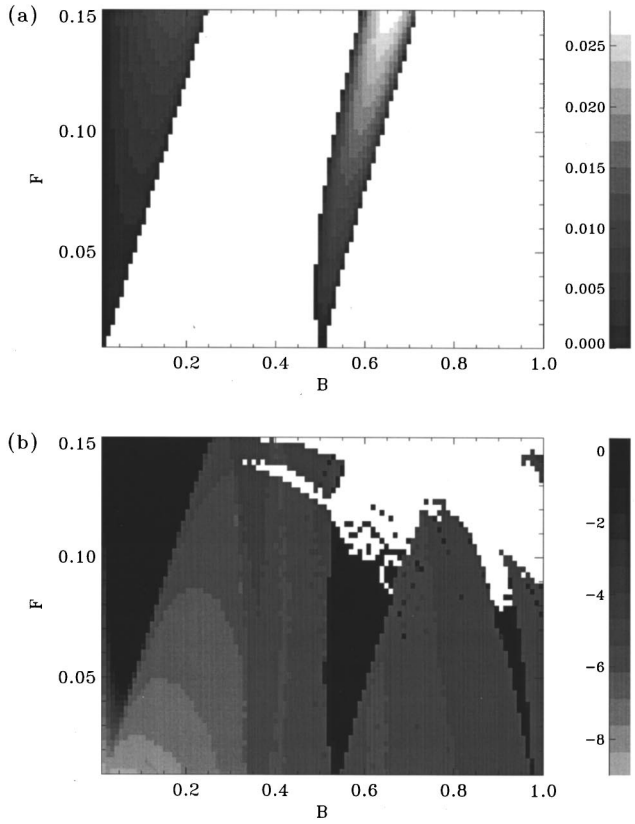

FIG. 12. Stability of the planar motion as a function of B and F at $E=-\frac{1}{2}$. (a) shows the maximum Lyapunov exponent for the P_s orbit of the normalized motion. Field values at which P_s is stable are plain white. Otherwise a bright shading denotes a large Lyapunov exponent. In (b), for the same fields values, the gray shading codes the logarithm of the maximum distance from the xy plane for a trajectory that is launched a very small distance from that plane. Here, dark regions mean instability of the motion with respect to the xy plane, while ionizing trajectories are white. Note that these methods are not sensitive to the stability of the motion *within* the xy plane.

B. Quantal manifestations of chaos

Investigations of eigenvalues statistics are a common means to find the signatures of classical mechanics in the corresponding quantum mechanical system. An example is given by the distribution of nearest-neighbor level spacings. Spectra for regular system in general follow the Poisson distribution [24], which shows its maximum at zero spacing between eigenenergies, while in the spectra of chaotic systems that are described by Wigner statistics [25] the probability for zero spacing vanishes.

For systems with a mixed phase space, a useful interpolation between these two extremes is given by the Brody distribution [26]

$$P_\beta(x)=ax^\beta e^{-bx^{\beta+1}},\quad 0\leqslant\beta\leqslant 1, \tag{32}$$

where a and b are normalizing factors [26]. For $\beta=0$, the Poisson distribution is recovered, while $\beta=1$ corresponds to the Wigner distribution.

Plotting, as a function of the fields, the parameter β that best fits this distribution to the level statistics of the normalizing Hamiltonian (6) reveals the influence of the lines of stability on the quantum spectra (Fig. 13). However, this is successful only for very strong magnetic fields, so that a comparison to the energy levels of the exact Hamiltonian is not possible.

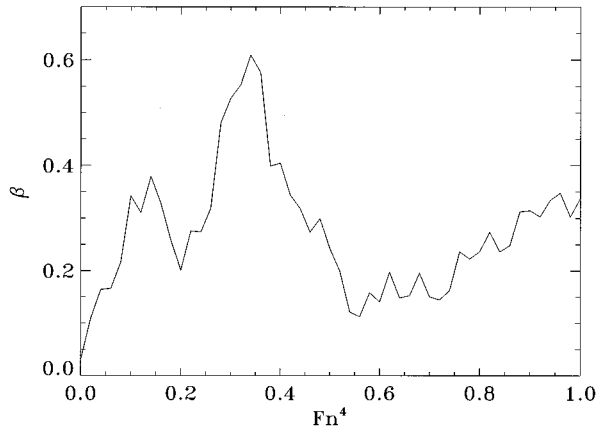

FIG. 13. Plotted as a function of Fn^4 (at $Bn^3=1$, $n=50$, odd parity) is the parameter β that best fits a Brody distribution to the nearest-neighbor energy level statistics of the normalized Hamiltonian (6). Note the minima of β at $Fn^4=0.2$ and $Fn^4=0.55$, implying a mostly Poissonian distribution, i.e., ''regular'' quantum spectra, located on the two lines of classical stability.

C. Coherent state analysis

One way to compare eigenstates of Hamiltonian (6) with the classical dynamics is to plot their coefficients in the J_zK_z basis and to overlay the projection onto J_zK_z space of the corresponding trajectory, which we have done in Fig. 14. This corresponds to comparing a trajectory in Cartesian space with the configuration space representation of a wave function.

A more appropriate way of comparing classical and quantum mechanics is to compute phase space projections of the wave function, e.g., the Husimi function of a wave function in configuration space, which is the projection of the wave function on minimum uncertainty Gaussian wave packets [27]. In the present case, we have to use the coherent states of the group $SU(2)\otimes SU(2)$.

SU(2) coherent states $|\theta_J\phi_J\rangle$ and $|\theta_K\phi_K\rangle$ for the angular momenta **J** and **K** are obtained [28] by rotating the minimum uncertainty state $|j-j\rangle$ through the angles θ_J and ϕ_J where

$$J_x=\frac{n}{2}\sin\theta_J\cos\phi_J,$$

$$J_y=\frac{n}{2}\sin\theta_J\sin\phi_J, \tag{33}$$

$$J_z=\frac{n}{2}\cos\theta_J,$$

and one obtains [29]

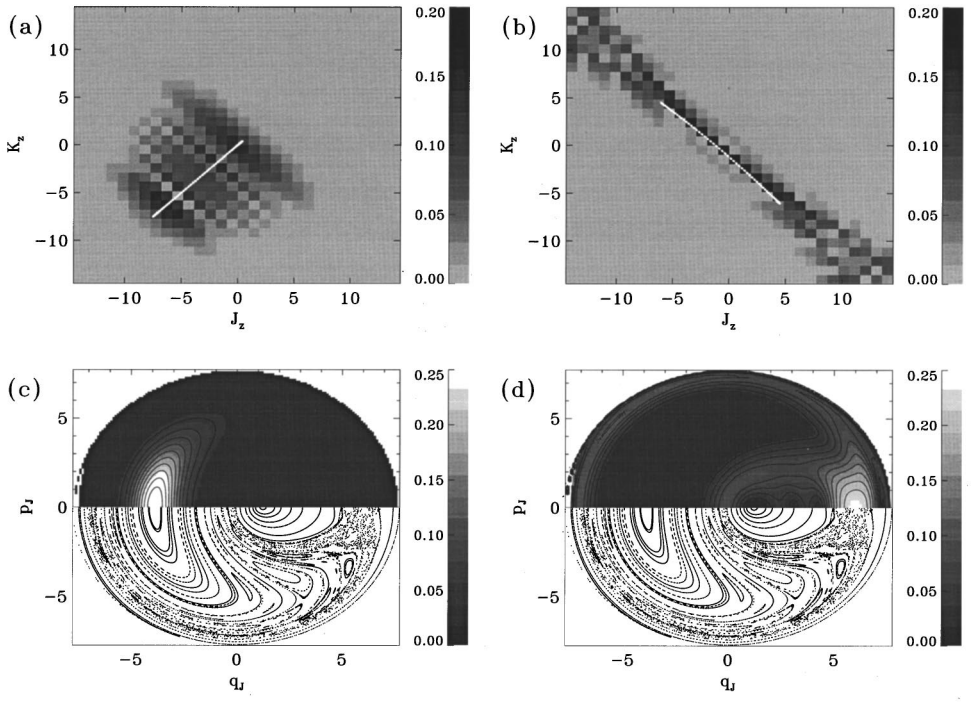

FIG. 14. Quantum mechanical eigenstates of the normalized Hamiltonian that follow the classical periodic orbits P_s (left) and P_u (right), with $n=30$, $B=0.45$, $F=0.045$. (a) and (b) show projections onto J_zK_z space. Due to the time reversal symmetry, these periodic orbits retrace themselves after a half period. For P_s, we have $J_z=K_z$. (c) and (d) show quantum surfaces of section (upper half). The corresponding PSOS is shown in the lower half. Note that the wave function in (d) extends along the separatrix, the unstable fixed point of which is P_u, avoiding regions of stable motion, and this wave function may be dubbed a quantum state in the intramanifold chaos. In contrast, the wave function in (b) extends over invariant tori in the vicinity of P_s only.

$$|\theta_J\phi_J\rangle=\sum_{m=-j}^{j}\begin{pmatrix}2j\\ j+m\end{pmatrix}^{1/2}\times\sin^{j+m}(\theta_J/2)\cos^{j-m}(\theta_J/2)e^{-i(j+m)\phi_J}|jm\rangle, \quad (34)$$

and similarly for **K**. **JK** coherent states, coherent states of the group SU(2)⊗SU(2), at given ''classical coordinates'' **J** and **K**, may then be formed as products of individual coherent states:

$$|\theta_J\phi_J,\theta_K\phi_K\rangle=|\theta_J\phi_J\rangle|\theta_K\phi_K\rangle. \quad (35)$$

Coherent states may now be used, e.g., to find the overlap of a wave function with a classical orbit. More importantly choosing the coherent states along the Poincaré surface of section, one obtains the so-called quantum surface of section (QSOS). Figure 14 displays QSOS's for wave functions that strongly overlap with the two basic periodic orbits P_s and P_u. The figure shows how the quantum states follow the underlying classical structures, i.e., the wave function that corresponds to P_u extends over the entire (intramanifold) chaotic region formed around P_u [Fig. 14(d)], while in Fig. 14(c), the wave function is restricted to the invariant tori in the vicinity of P_s.

VI. CONCLUSIONS

We have shown that the exact Hamiltonian of a Rydberg electron in crossed electric and magnetic fields can be usefully approximated by combining the normal form theory, the classical perturbation theory, and Lie algebra. Despite the enormous size of the parameter and phase space of the original Hamiltonian, the normalized Hamiltonian gives a clear view of the nonlinear dynamics, the structure of phase space, its periodic motions, and chaos-order alternations. It describes that part of the dynamics that appears to determine the ''physics'' of the motion, namely, the evolution of Kepler ellipses under the influence of the external fields. The special status assigned to certain dominant periodic orbits by experimental photoabsorption spectra emerges naturally from our treatment.

By comparing our results with those of exact dynamics, we see that the normalized Hamiltonian represents a very valuable guide to the properties of the exact motion, making accurate predictions for low fields, classically as well as quantum mechanically.

In particular, the normalized Hamiltonian shows how an electric field induces the onset of chaotic motion: even small values of F cause chaos when a magnetic field alone is not sufficient to obtain visible chaos. This intramanifold chaos is linked to the stability of a simple periodic orbit (P_u). Chaos emerges from the middle of an n manifold and vanishes again when P_u becomes stable. In addition, this Hamiltonian can predict the location of regions of regular and chaotic motion; surprisingly, the induced structure remains valid for high fields.

ACKNOWLEDGMENTS

J.v.M. is grateful to the Alexander von Humboldt Foundation for financial support. We thank the National Science Foundation for its support of this research.

[1] M. Born, *The Mechanics of the Atom* (Ungar, New York, 1960), pp. 235–241.
[2] T. F. Gallagher, *Rydberg Atoms* (Cambridge University Press, Cambridge, 1994).
[3] H. Friedrich and D. Wintgen, Phys. Rep. **183**, 37 (1989).
[4] G. Raithel, M. Fauth, and H. Walther, Phys. Rev. A **44**, 1898 (1991).
[5] G. Raithel, M. Fauth, and H. Walther, Phys. Rev. A **47**, 419 (1993).
[6] D. Delande and J.-C. Gay, in *The Hydrogen Atom*, edited by G. Bassani, M. Inguscio, and T. Haensch (Springer-Verlag, Berlin, 1989), pp. 323–334.
[7] M. L. Zimmerman, M. M. Kash, and D. Kleppner, Phys. Rev. Lett. **45**, 1092 (1980).
[8] J. von Milczewski, G. H. F. Diercksen, and T. Uzer, Phys. Rev. Lett. **76**, 2890 (1996).
[9] J. A. Yeazell *et al.*, Phys. Rev. Lett. **70**, 2884 (1993).
[10] M. J. Gourlay, T. Uzer, and D. Farrelly, Phys. Rev. A **47**, 3113 (1993); **48**, 2508(E) (1993).
[11] P. Schmelcher and L. S. Cederbaum, Phys. Rev. A **47**, 2634 (1993).
[12] M. J. Englefield, *Group Theory and the Coulomb Problem* (Wiley-Interscience, New York, 1972).
[13] J. C. Gay, in *Progress in Atomic Spectroscopy, Part C*, edited by H. J. Beyer and H. Kleinpoppen (Plenum, New York, 1984), p. 177.
[14] J. von Milczewski, Doctoral dissertation, Technical University of Munich, 1995 (unpublished).
[15] E. A. Solov'ev, Zh. Eksp. Teor. Fiz. **82**, 1762 (1982) [Sov. Phys. JETP **55**, 1017 (1982)].
[16] J. A. G. Roberts and G. R. W. Quispel, Phys. Rep. **216**, 63 (1992).
[17] J. von Milczewski, G. H. F. Diercksen, and T. Uzer, Phys. Rev. Lett. **73**, 2428 (1994).
[18] H. Hasegawa, M. Robnik, and G. Wunner, Prog. Theor. Phys. **98**, 198 (1989).
[19] A. J. Lichtenberg and M. A. Lieberman, *Regular and Chaotic Dynamics* (Springer-Verlag, New York, 1992).
[20] J. Main, Ph.D. thesis, Universität Bielefeld, 1991 (unpublished).
[21] C. W. Clark and K. T. Taylor, J. Phys. B **15**, 1175 (1982).
[22] D. Delande and J. C. Gay, J. Phys. B **17**, L335 (1984).
[23] M. L. Zimmerman, M. G. Littman, M. M. Kash, and D. Kleppner, Phys. Rev. A **20**, 2251 (1979).
[24] M. V. Berry and M. Tabor, Proc. R. Soc. London, Ser. A **356**, 375 (1977).
[25] O. Bohigas and M. J. Giannoni, in *Mathematical and Computational Methods in Nuclear Physics*, edited by J. S. Dehesa *et al.*, Lecture Notes in Physics Vol. 209 (Springer-Verlag, Berlin, 1984), p. 1.
[26] T. A. Brody *et al.*, Rev. Mod. Phys. **53**, 385 (1981).
[27] F. Haake, *Quantum Signatures of Chaos* (Springer-Verlag, Berlin, 1991).
[28] W.-M. Zhang, D. H. Feng, and R. Gilmore, Rev. Mod. Phys. **62**, 867 (1990).
[29] C. C. Martens, J. Chem. Phys. **96**, 1870 (1992).